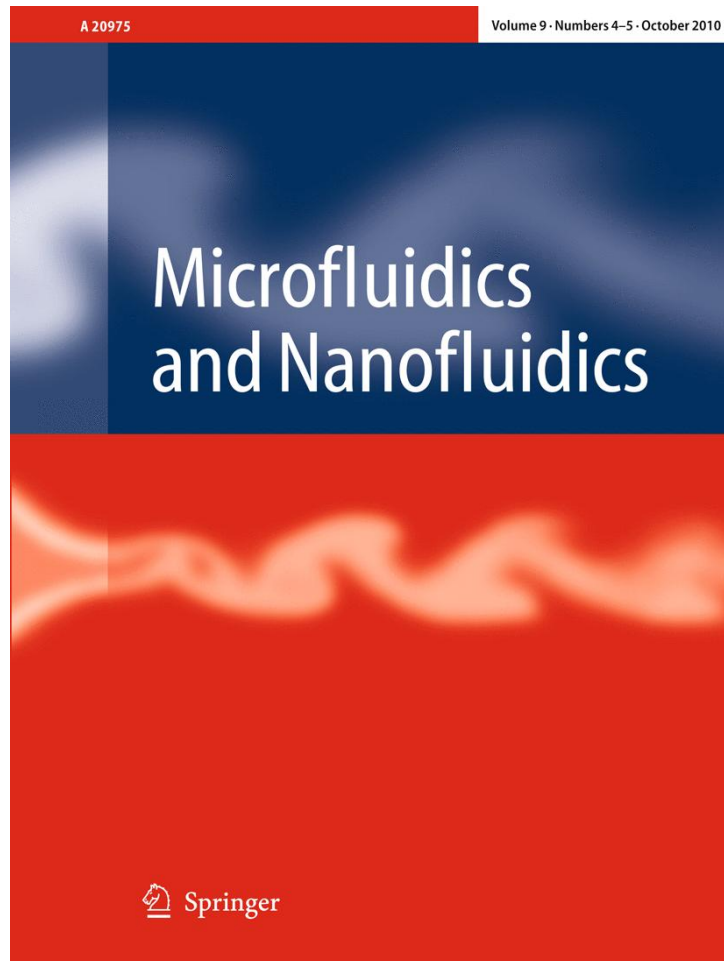


ISSN 1613-4982, Volume 9, Combined 4-5



**This article was published in the above mentioned Springer issue.
The material, including all portions thereof, is protected by copyright;
all rights are held exclusively by Springer Science + Business Media.
The material is for personal use only;
commercial use is not permitted.
Unauthorized reproduction, transfer and/or use
may be a violation of criminal as well as civil law.**

An analytical formula and FEM simulations for the viscous damping of a periodic perforated MEMS microstructure outside the lubrication approximation

Dorel Homentcovschi · Bruce T. Murray ·
Ronald N. Miles

Received: 12 January 2010 / Accepted: 10 March 2010 / Published online: 2 April 2010
© Springer-Verlag 2010

Abstract The article presents an axi-symmetrical model for determining the total damping coefficient of a periodic perforated microelectromechanical systems (MEMS) microstructure for cases where the lubrication approximation yielding the Reynolds' equation is no longer appropriate. Damping is modeled by solving for the viscous flow in an approximation of the periodic cell geometry using an equivalent axi-symmetrical cylindrical flow domain. Using the Stokes approximation of the incompressible Navier–Stokes (N–S) equations with harmonic time behavior, an analytic solution is obtained yielding an explicit formula for the damping coefficient. Additionally, two numerical models were implemented based on the finite element method. Numerical solutions were obtained for the linearized, viscous acoustic equations (time harmonic) and the steady, incompressible N–S equations. The results given by the analytical formula compare well with those obtained from the FEM solutions and with measured values for MEMS microstructures found in the literature.

Keywords Perforated microstructures · Viscous damping · MEMS microphones · Navier–Stokes equations

1 Introduction

The study of a thin air layer squeezed between a moving plate and a rigid plate, referred to as a planar

microstructure, is important in many microelectromechanical systems (MEMS) such as microphones (Berquist 1993), microaccelerometers (Gerlach-Mayer 1991), resonators (Mattila et al. 2000), tunable microoptical interferometers (Wu et al. 1996), etc. The horizontal motion of the thin air gap in a planar microstructure yields squeeze-film damping that can adversely affect the dynamic response of the device (Bao and Yang 2000). On the other hand, many MEMS devices need to be damped for stable operation, as in the case of a lightly damped micromachined accelerometer that can be destroyed by large deflections of its proof mass due to mechanical shock. Thus, viscous damping is a critical factor for many MEMS transducers. As a result there is an extensive literature dedicated to the study of squeeze-film damping in the MEMS area (Škvor 1967; Starr 1990; Veijola 2006a; Bao and Yang 2007). Much of the existing work is based on analytical or numerical integration of the Reynolds' equation.

The perforations in one of the plates (e.g., the backplate in case of microphones or the proofmass for accelerometers) can be used to control the viscous damping. The rigid backplate often contains perforations for reducing the time required to remove sacrificial materials between the moving structure and backplate during the wet etching process. Squeeze-film damping is reduced by incorporating holes in one (or both plates). However, the vertical motion of the air within the holes gives a new viscous resistance which adds to the squeeze-film damping. A rigorous treatment of the total damping problem requires the solution of the Navier–Stokes (N–S) equations (or linearized forms, e.g., viscous acoustic equations, Stokes approximation) in the 3-D domain consisting of the gap between the plates and the volume of the holes, which is difficult for a geometrically complex MEMS structure. Accurate three-dimensional (3-D) flow simulations are not practical for the entire

D. Homentcovschi (✉) · B. T. Murray · R. N. Miles
Department of Mechanical Engineering, SUNY Binghamton,
Binghamton, NY 13902-6000, USA
e-mail: homentco@binghamton.edu

D. Homentcovschi
"Politehnica" University of Bucharest, Bucharest, Romania

microstructure geometry (Veijola 2006a) due to the computational resources required.

The lubrication approximation applies when the distance between the plane surfaces is sufficiently small. This assumption makes it possible to integrate the N–S equations over the separation distance and yields the Reynold's equation. In the case of perforated microstructures, the assumption that the flow domain is thin is not necessarily valid in the region of the holes. As a result, the Reynold's equation cannot be applied unless the pitch of the holes is much larger than the distance between plates and the diameter of the holes, which is not the case in many applications.

There are two ways to overcome the difficulties associated with the application of the Reynold's equation for perforated microstructures. The first one is to modify the Reynold's equation by adding new terms and coefficients to account for the influence of the holes to the pressure of the flow through the microstructure (Veijola and Mattila 2001; Bao et al. 2003; Mohite et al. 2008). This approximation turns the actual 3-D problem into a 2-D one that is much more amenable to analytical investigations and numerical simulations. The modified Reynold's equation has been solved analytically in particular cases. More complicated domains require the use of numerical methods. In the “analytic damping model” derived by Veijola (2006a, b) (see also Veijola and Raback 2007; Mohite et al. 2005; Pandey and Pratap 2005) the mechanical resistance of a perforation cell consists of six lumped flow resistances. One of these resistances is derived analytically using the Reynold's equation. The elongations involved in the other lumped resistances contain up to 20 numerical coefficients that are determined using some heuristic arguments and fitting to Finite Element Method (FEM) simulations. All the methods developed for determining the damping force of oscillating perforated microstructures obtained by extending the Reynold's equation are known as “compact models.” As noted in the recent articles by Veijola et al. (2008, 2009) “the verification of the compact models is generally questionable.”

An alternate way to determine the viscous damping of perforated microstructures, for cases outside of the validity of the Reynold's equation, is to directly integrate the N–S equations and obtain the velocity and pressure fields. This approach is especially attractive when it is possible to take advantage of the repetitive pattern of holes which is typical in most designs. The periodic pattern of holes can be modeled in terms of a single basic cell associated with each hole. The region of air beneath the hole (inside the gap) is generally a hexagonal or square prism. Due to symmetry, the normal velocity on each side plane of these prisms vanishes. Here, the prismatic part of the basic cell will be approximated by a circular cylinder (of the same section

area and height) having zero normal velocity along the lateral surface. This configuration changes the 3-D solution domain for the basic cell into a 2-D, axi-symmetrical one. Using this domain simplification, the analysis of viscous damping for the original periodic microstructure can be performed by solving the governing equations and computing the pressure and velocity fields using both analytical and numerical methods.

The analytical method presented in Sect. 3, is based on using the Stokes approximation to the N–S equations (with harmonic time dependence) to describe the motion of the incompressible fluid in the approximated cell. Here, this approach yields a compact formula for the total damping coefficient of a cell B (defined as the total pressure on the diaphragm inside the cell divided by its average normal velocity) when the pitch of the holes $l = 2b$, the hole radius r , and the gap d have comparable geometrical dimensions. This formula extends the classical result obtained by Skvor on the basis of the lubrication approximation (Bao 2000; Homentcovschi and Miles 2004).

In Sect. 4, the FEM is employed to solve for the flow in a representative axi-symmetric domain and determine the viscous damping. The numerical solution approach is used to solve the governing equations for two different models: the linearized, compressible N–S equations assuming harmonic time variation (linearized viscous acoustic equations) and the incompressible N–S equations assuming steady behavior. The steady N–S model is independent of frequency. The results presented show that the assumption of steady, incompressible flow yields useful results for small to medium frequencies. The variation in model assumptions between the analytical model and the two numerical models will provide insight into the roles played by the different physical effects (i.e., nonlinear inertia terms, time dependence, compressibility). The numerical results are more broadly applicable and are valid in the case of larger holes. The analytical approach yields a formula for the damping coefficient which provides insight and is convenient to use. The FEM solutions require the specification of model parameter values and a number of simulations must be run to analyze the behavior of the two computational models (i.e., steady-state motion for an incompressible fluid versus harmonic time-dependence for a compressible fluid). A comparison of the results from all three models at the end of the section shows that the analytical formula provides a good approximation for the damping coefficient over a broad range of frequencies.

In Sect. 5, the analytical and FEM results for the damping coefficient are compared with predictions based on the Reynold's equation for squeezed-film damping (modified to include the resistance of the holes). The comparison yields insight into the limits of applicability of the (Reynold's equation-based) compact models. The

analytical and numerical results presented here show that models based on the Reynold's equation applied in the gap domain yield reasonable results only if the distance between the holes in the periodic array is at least 20 times larger than the radius of the holes or, in the case of small hole radius, if the thickness of the backplate is sufficiently large.

In Sect. 6, the damping coefficients obtained using the analytical formula and from the FEM computations are compared to the measured coefficient values of some particular perforated microstructures provided by Somà and De Pasquale (2007, 2008) and De Pasquale et al. (2010). The results given by the analytical method and FEM models are found to compare well with the measured values, and are found to be in much better agreement with the measured damping coefficients as compared to the predictions obtained from compact models (Veijola et al. 2008, 2009).

For the viscous damping problem, the results of this work can be applied for cases when the Reynolds' equation is not appropriate, i.e., when the pitch of holes, the gap, and the diameter of holes have comparable geometrical dimensions.

2 Geometry and model formulations

2.1 Axi-symmetric domain approximation

Consider a uniformly perforated microstructure with a repetitive pattern of holes (fixed pitch and hole diameter). In the case of a staggered pattern of holes, an hexagonal pattern repeats while for aligned (nonstaggered) holes a square pattern results (see Fig. 1a). The upper plate is the perforated backplate (of thickness h) and the lower one is the diaphragm. The distance d between the average positions of the two plates is the air gap of the structure. The circular cylindrical holes (of radius r and height h) lie on the vertices of a regular lattice of hexagons or squares with side length denoted by $l = 2b$ (b is the half-period of the lattice) in both the cases. The air domain in the case of aligned holes (square pattern) is shown in Fig. 1b. The repetitive pattern of the system of holes and the vertical motion of the diaphragm impose a similarly repetitive

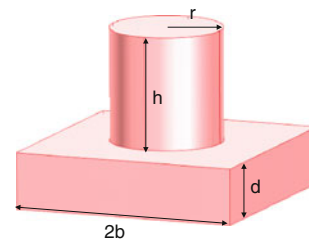
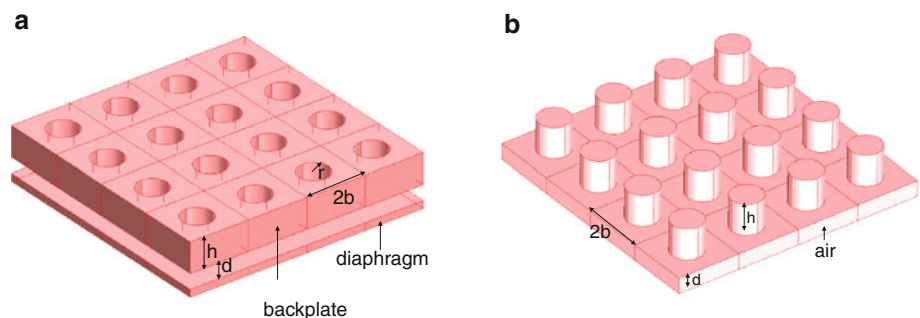


Fig. 2 A basic element of a periodic planar microstructure

response in the motion of the air. The actual domain for a single repeating cell is shown in Fig. 2. It consists of a square (or hexagonal prism in the case of staggered holes) lower domain region D_g located below the cylindrical part of the domain D_h representing the hole. All the side planes of the domain D_g are symmetry planes for the fluid motion. Consequently, on each symmetry plane the normal component of velocity and the normal pressure derivative are zero. On the solid boundary surfaces of D_g and the hole, the velocity components vanish (no slip and no penetration conditions). Finally, the pressure equals the external (atmospheric pressure) on the upper surface of the hole and the vertical velocity on the lower part of D_g is prescribed.

In order to simplify the problem we approximate the lower region of the basic cell domain D_g by a circular cylinder C_g (as shown in Fig. 3a) of the same volume and with the area of the normal section equal to the area of the hexagonal or square section of the prism D_g . The radius of the cylinder C_g is therefore $R = 2b\sqrt{\sqrt{3}/(2\pi)} = 1.128b$ in the case of staggered holes and $R = 2b/\sqrt{\pi} = 1.05b$ in the case of aligned holes. This domain configuration yields an axi-symmetrical problem rather than a fully 3-D one and is easier to treat both analytically and numerically. The axi-symmetric fluid domain is shown in Fig. 3a, b with dimensions and boundary conditions labeled. A cylindrical polar coordinate system (ρ, z) is used where ρ is the radial coordinate and z is the axial coordinate. The origin is placed such that the z -axis is the symmetry line of the cell in the center of the circular hole with $z = 0$ being the lower base of the cell. The radius of the hole is designated by r and as defined above the radius of the gap region is R . Due

Fig. 1 a A perforated planar microstructure. b The air domain corresponding to the planar microstructure



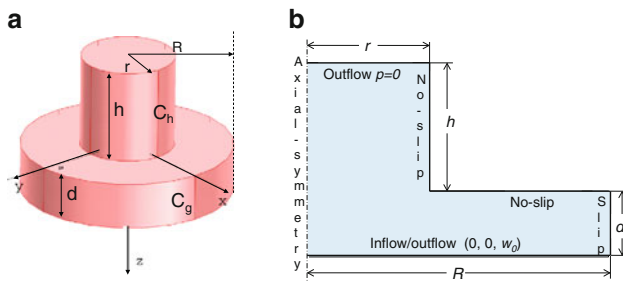


Fig. 3 **a** The cylindrical approximation of the gap domain of a basic element. **b** An axial section of the cylindrical approximation of the basic domain (cell)

to the periodic structure of the cell domain, the normal velocity is assumed to vanish on the side surface of the domain C_g . This approximation is appropriate in the case of small and moderate values of the area ratio A (defined as the ratio of the cross-sectional area of the hole over the total cross-sectional area of the domain D_g).

In certain applications, the MEMS microstructure has a regular pattern of square holes (width $2a$). The radius r_e of an equivalent cylindrical hole is obtained by equating the total resistance (sum of the direct and indirect resistances) from Homencovschi and Miles (2007) for circular and square holes, which yields $r_e = 1.094a$.

2.2 N–S and viscous acoustic equations

As discussed previously, when the thickness of the gap is comparable to the plane dimensions of the cell, the lubrication approximation can no longer be used. In the most general case, the flow of the viscous compressible fluid (characterized by the velocity field \mathbf{V} , the density $\tilde{\rho}$ and the pressure P) is governed by the compressible N–S system of equations

$$\frac{\partial \tilde{\rho}}{\partial t} + \mathbf{V} \cdot \nabla \tilde{\rho} + \tilde{\rho} \nabla \cdot \mathbf{V} = 0, \quad (1)$$

$$\tilde{\rho} \left[\frac{\partial \mathbf{V}}{\partial t} + (\mathbf{V} \cdot \nabla) \mathbf{V} \right] = \nabla \left(-P + \frac{\mu}{3} \nabla \cdot \mathbf{V} \right) + \mu \nabla^2 \mathbf{V}, \quad (2)$$

where μ is the shear viscosity. In the case of small gaps and high thermal conductivity of the walls the temperature can be assumed as constant (isothermal assumption). To close the system of Eqs. 1 and 2 an equation of state must be specified $\tilde{\rho} = \tilde{\rho}(P)$.

For small harmonic oscillations about a steady-state solution with zero velocities the dependent variables can be assumed to take the form

$$\mathbf{V} = \mathbf{v} e^{-i\omega t}, \quad P = p_0 + p e^{-i\omega t}, \quad \tilde{\rho} = \rho_0 + \rho' e^{-i\omega t}, \quad (4)$$

where p_0 and ρ_0 are constants in space and $\omega = 2\pi f$, f being the frequency. After inserting the above form of the

dependent variables into the governing equations and neglecting the quadratic terms in the dependent variables, the linearized viscous acoustics equations are obtained.

$$-\frac{i\omega}{p_0} p + \nabla \cdot \mathbf{v} = 0, \quad (5)$$

$$-i\omega \rho_0 \mathbf{v} = -\nabla \left(p - \frac{\mu}{3} \nabla \cdot \mathbf{v} \right) + \mu \Delta \mathbf{v}, \quad (6)$$

The constants p_0 and ρ_0 are connected by means of the relationship

$$p_0 = \rho_0 c_0^2, \quad (7)$$

c_0 being the isothermal speed of sound.

3 Analytic solution approach

For the case of an incompressible fluid, the system of Eqs. 5 and 6 coincides with the Stokes approximation to the N–S equations where the nonlinear inertia terms are neglected.

$$\nabla \cdot \mathbf{v} = 0, \quad (8)$$

$$i\omega \rho_0 \mathbf{v} + \mu \Delta \mathbf{v} = \nabla p, \quad (9)$$

The boundary conditions on the gap walls are specified by

$$u(\rho, 0) = 0, \quad u(\rho, d) = 0, \quad (10)$$

$$w(\rho, 0) = w^{(0)}(\rho), \quad w(\rho, d) = w^d(\rho), \quad (11)$$

where $(u(\rho, z), 0, w(\rho, z))$ are the components of the velocity field \mathbf{v} in cylindrical coordinates (ρ, φ, z) and the function $w^{(0)}(\rho)$ is nonzero only along the opening

$$w^{(0)}(\rho) = \begin{cases} \tilde{w}^{(0)}(\rho) & \text{if } \rho < r \\ 0 & \text{otherwise} \end{cases}, \quad (12)$$

$\tilde{w}^{(0)}(\rho)$ is a function to be specified later. The method can be applied in the case of arbitrary motion of the diaphragm. However in this work only the case of a rigid diaphragm in translational motion $w^d(\rho) \equiv w^d$ will be considered.

In solving the boundary-value problem the geometry of the domain is considered fixed, with the line $z = d$ corresponding to the average position of the vibrating plate. Such an approximation holds only for small amplitude oscillations of the diaphragm. This is generally the case for microphones, microaccelerometers, tunable micro-optical interferometers, etc.

The boundary conditions Eqs. 10–12 include the no-slip boundary conditions assuming a continuum flow. If the channel dimensions approach the mean-free path of the air, then the decreased pressure (rarefaction effect) may change the boundary conditions on the solid surfaces yielding slip (nonzero tangential velocity) of the fluid particles. As the scale of the flow is very small a slip model may be appropriate. However, if the pitch of holes is on the order of the air gap, the presence of holes reduces the possibility

of slip on the solid surfaces of the microstructure. For a gap on the order of 1 μm and an area ratio, A (area of the hole divided by the total area of the cylindrical gap region), of around 50%, half of the working area is open. Thus, the effective gap of the structure is much larger than 1 μm and rarefied gas behavior should not be important. The presence of holes gives a redistribution of the pressure on the backplate very different from rarefaction conditions in a small gap between two parallel, nonperforated plane surfaces where a slip-flow is a better model. The pressure release from the hole may be dominant when compared to pressure reduction due to rarefaction, which is the assumption adopted in this article. However, a more precise model has to consider some slip of the flow over solid walls determined by the balance between pressure release do to the holes and rarefaction. The proper importance of these two opposite influences is an open problem.

In Veijola et al. (2008, 2009) both no-slip (models $M1$ and $M2$) and models with a slip velocity boundary condition ($M3$ and $M4$) were used along the walls in the air gap and the hole. The results given in Table III in Veijola (2008) are closer to the measured (experimental) values when the standard continuum no-slip condition is applied along the solid surfaces.

3.1 Vorticity/pressure formulation

Equation 9 can be rewritten as:

$$\mathbf{v} = \frac{1}{i\omega\rho_0}\nabla p - \frac{\mu}{i\omega\rho_0}\Delta\mathbf{v}. \tag{13}$$

Using the vector identity

$$\nabla \times (\nabla \times \mathbf{v}) = \nabla(\nabla \cdot \mathbf{v}) - \Delta\mathbf{v}, \tag{14}$$

and taking into account the continuity equation for an incompressible fluid Eq. 8, we obtain

$$\mathbf{v} = \frac{1}{i\omega\rho_0}\nabla p + \frac{\mu}{i\omega\rho_0}\nabla \times \mathbf{\Omega}, \tag{15}$$

where the vorticity $\mathbf{\Omega}$ is defined by

$$\mathbf{\Omega} = \nabla \times \mathbf{v}. \tag{16}$$

For the axi-symmetrical case, in cylindrical coordinates (ρ, φ, z) , there is only one vorticity component

$$\nabla \times \mathbf{v} = \mathbf{\Omega}\hat{\varphi}. \tag{17}$$

Thus, we obtain expressions for the velocities in terms of the pressure and vorticity vector as potentials

$$\mathbf{v} = \frac{1}{i\omega\rho_0}\nabla p + \frac{\mu}{i\omega\rho_0}\nabla \times (\mathbf{\Omega}\hat{\varphi}). \tag{18}$$

The velocity components for axi-symmetrical flow written in cylindrical coordinates are given by

$$u(\rho, z) = \frac{1}{i\omega\rho_0}\frac{\partial p}{\partial \rho} - \frac{\mu}{i\omega\rho_0}\frac{\partial \mathbf{\Omega}}{\partial z}, \tag{19}$$

$$w(\rho, z) = \frac{1}{i\omega\rho_0}\frac{\partial p}{\partial z} + \frac{\mu}{i\omega\rho_0}\frac{1}{\rho}\frac{\partial(\rho\mathbf{\Omega})}{\partial \rho}, \tag{20}$$

where $u(\rho, z)$ is the radial component and $w(\rho, z)$ is the axial component of velocity. Expressing the operators $\nabla \cdot$ and $\nabla \times$ in cylindrical coordinates and applying the relationships (8) and (17), we obtain the following two equations for the pressure and vorticity fields

$$\frac{1}{\rho}\frac{\partial}{\partial \rho}\left(\rho\frac{\partial p}{\partial \rho}\right) + \frac{\partial^2 p}{\partial z^2} = 0, \tag{21}$$

and

$$\frac{1}{\rho}\frac{\partial}{\partial \rho}\left(\rho\frac{\partial \mathbf{\Omega}}{\partial \rho}\right) - \frac{\mathbf{\Omega}}{\rho^2} + \frac{\partial^2 \mathbf{\Omega}}{\partial z^2} + \frac{i\omega\rho_0}{\mu}\mathbf{\Omega} = 0. \tag{22}$$

3.2 Separation of variables solution

Because Eqs. 21 and 22 are linear and the boundary conditions along the external cylindrical surface are homogeneous, separation of variables can be used to obtain the solution,

$$\frac{1}{i\omega\rho_0}p(\rho, z) = \phi_0(z) + \sum_{n=1}^{\infty} \phi_n(z)J_0(q_n\rho) \tag{23}$$

where

$$\begin{aligned} \phi_0(z) &= A_0 + B_0z, \\ \phi_n(z) &= A_n \cosh(q_nz) + B_n \sinh(q_nz), \end{aligned} \tag{24}$$

and the eigenvalues q_n are determined by

$$J_1(q_nR) = 0, \quad n = 0, 1, 2, \dots \tag{25}$$

Similarly, the solution for the vorticity has the form

$$\frac{\mu}{i\omega\rho_0}\mathbf{\Omega}(\rho, z) = \sum_{n=1}^{\infty} \mathbf{\Omega}_n(z)J_1(q_n\rho) \tag{26}$$

with the eigenfunctions and eigenvalues given by

$$\begin{aligned} \mathbf{\Omega}_n(z) &= C_n \cosh(r_nz) + D_n \sinh(r_nz), \\ r_n &= \sqrt{q_n^2 - \frac{i\omega\rho_0}{\mu}}. \end{aligned} \tag{27}$$

Equations 19 and 20 yield the following representation formulas for the components of the velocity field

$$u(\rho, z) = \sum_{n=1}^{\infty} u_n(z)J_1(q_n\rho), \tag{28}$$

where

$$\begin{aligned} u_n(z) &= -q_n[A_n \cosh(q_nz) + B_n \sinh(q_nz)] \\ &\quad - r_n[C_n \sinh(r_nz) + D_n \cosh(r_nz)], \end{aligned} \tag{29}$$

and

$$w(\rho, z) = B_0 + \sum_{n=1}^{\infty} w_n(z) J_0(q_n \rho). \quad (30)$$

The function $w_n(z)$ is given by

$$w_n(z) = q_n [A_n \sinh(q_n z) + B_n \cosh(q_n z)] + q_n [C_n \cosh(r_n z) + D_n \sinh(r_n z)]. \quad (31)$$

The constants $A_0, B_0, A_n, B_n, C_n, D_n$ are determined from applying the boundary conditions as described below.

3.3 Determination of series constants

Let $w_n^{(0)}$ and $w_n^{(d)}$ denote the Fourier Bessel series expansions coefficients of the functions $\tilde{w}^{(0)}(\rho)$ and $w^{(d)}(\rho)$, respectively:

$$w_n^{(0)} = \frac{2}{R^2} \int_0^r \tilde{w}^{(0)}(\rho) \rho \frac{J_0(q_n \rho)}{J_0^2(q_n R)} d\rho, \quad (32)$$

$$w_n^{(d)} = \frac{2}{R^2} \int_0^R w^{(d)}(\rho) \rho \frac{J_0(q_n \rho)}{J_0^2(q_n R)} d\rho, \quad (33)$$

for $n = 1, 2, \dots$. For $n = 0$, the conditions for the velocity component w along the planes $z = 0$ and $z = d$ give

$$B_0 = w_0^{(0)} = \frac{r^2}{R^2} w^{(0)} \quad (34)$$

$$B_0 = w_0^{(d)} = w^{(d)}. \quad (35)$$

Combining Eqs. 34 and 35 yields the following expression

$$w^{(0)} = \frac{R^2}{r^2} w^{(d)}$$

where R is the equivalent radius of a cell and r the hole radius. Multiplying by Eq. 30 by ρ and integrating over the interval $[0, R]$ the relationship (31) gives

$$Q_0 \equiv 2\pi \int_0^R \rho w(\rho, d) d\rho = \pi R^2 B_0.$$

Using the same procedure on Eq. 23 yields

$$P_0 \equiv 2\pi \int_0^R \rho p(\rho, d) d\rho = i\omega \rho_0 \pi R^2 [A_0 + B_0 d],$$

Q_0 being the rate of flow and P_0 the total pressure on the base of the cell. Finally, using the above expression for P_0 and Eq. 35 we obtain

$$B_0 = w^{(d)}, \quad A_0 = \frac{P_0}{i\omega \rho_0 \pi R^2} - \frac{w^{(d)}}{\pi R^2} d.$$

Along the plane $z = d$ we can write

$$q_n [A_n \cosh(q_n d) + B_n \sinh(q_n d)] + r_n [C_n \sinh(r_n d) + D_n \cosh(r_n d)] = 0 \quad (36)$$

$$q_n [A_n \sinh(q_n d) + B_n \cosh(q_n d)] + q_n [C_n \cosh(r_n d) + D_n \sinh(r_n d)] = w_n^{(d)} \quad (37)$$

Similarly, along the plane $z = 0$ the u and w components of the velocity give

$$q_n A_n + r_n D_n = 0 \quad (38)$$

$$q_n B_n + q_n C_n = w_n^{(0)} \quad (39)$$

$w_n^{(0)}$ are the Fourier Bessel expansion coefficients corresponding to the functions defined by Eq. 12. Equations 36–39 determine all the remaining coefficients as

$$A_n = \mathbb{A}_n^{(0)} w_n^{(0)} + \mathbb{A}_n^{(d)} w_n^{(d)}, \quad (40)$$

$$B_n = \mathbb{B}_n^{(0)} w_n^{(0)} + \mathbb{B}_n^{(d)} w_n^{(d)}, \quad (41)$$

The operators $\mathbb{A}_n^{(0)}, \dots, \mathbb{B}_n^{(d)}$ are defined by formulas

$$\mathbb{A}_n^{(0)} = \frac{\sinh(q_n d) \cosh(r_n d) - r_n q_n^{-1} \cosh(q_n d) \sinh(r_n d)}{q_n [2 - 2 \cosh(q_n d) \cosh(r_n d) + [q_n r_n^{-1} + r_n q_n^{-1}] \sinh(q_n d) \sinh(r_n d)]}, \quad (42)$$

$$\mathbb{A}_n^{(d)} = \frac{r_n q_n^{-1} \sinh(r_n d) - \sinh(q_n d)}{q_n [2 - 2 \cosh(q_n d) \cosh(r_n d) + [q_n r_n^{-1} + r_n q_n^{-1}] \sinh(q_n d) \sinh(r_n d)]}, \quad (43)$$

$$\mathbb{B}_n^{(0)} = \frac{1 - \cosh(q_n d) \cosh(r_n d) + r_n q_n^{-1} \sinh(q_n d) \sinh(r_n d)}{q_n [2 - 2 \cosh(q_n d) \cosh(r_n d) + [q_n r_n^{-1} + r_n q_n^{-1}] \sinh(q_n d) \sinh(r_n d)]}, \quad (44)$$

$$\mathbb{B}_n^{(d)} = \frac{\cosh(q_n d) - \cosh(r_n d)}{q_n [2 - 2 \cosh(q_n d) \cosh(r_n d) + [q_n r_n^{-1} + r_n q_n^{-1}] \sinh(q_n d) \sinh(r_n d)]}. \quad (45)$$

3.4 Analytic expression for the total force

We assume that at the lower base of a hole (in the opening) the pressure has the form

$$p(\rho, 0) = p^{(0)}, \quad \rho < r. \tag{46}$$

Also, the axial velocity is

$$w(\rho, 0) \equiv \tilde{w}^{(0)}(\rho) = w^{(0)}, \quad \rho < r \tag{47}$$

corresponding to a constant velocity in the opening and $w(\rho, 0) = 0$ on the rest of the plane $z = 0$ inside the cell. The one-term approximations Eq. 46 for the pressure and Eq. 47 for velocity assume small values of the radius r . For larger holes more terms have to be considered involving more unknown coefficients. However it will be shown in the applications section that the one-term approximation works well even in the case of medium sized holes.

The equations of the problem are obtained now using the condition (46)

$$A_0 - \frac{p^{(0)}}{i\omega\rho_0} + \sum_{n=1}^{\infty} A_n J_0(q_n \rho) = 0, \quad \rho < r. \tag{48}$$

Equation 48 can be integrated with respect to ρ yielding

$$A_0 \frac{\rho}{2} - \frac{p^{(0)}\rho}{i\omega\rho_0 2} + \sum_{n=1}^{\infty} \frac{A_n}{q_n} J_1(q_n \rho) = 0, \quad \rho < r. \tag{49}$$

Using Eq. 49 and the formulas (40) and (41) we obtain

$$\sum_{n=1}^{\infty} \left[\frac{\mathbb{A}_n^{(0)}}{q_n} w_n^{(0)} + \frac{\mathbb{A}_n^{(d)}}{q_n} w_n^{(d)} \right] J_1(q_n \rho) = -A_0 \frac{\rho}{2} + \frac{p^{(0)}\rho}{i\omega\rho_0 2} \quad \rho < r. \tag{50}$$

Correspondingly, the formulas (32), (33), (64), and (67) give

$$w_n^{(0)} = w^{(0)} \frac{2r}{R^2} \frac{J_1(q_n r)}{J_0^2(q_n R) q_n}, \quad w_n^{(d)} = w^{(d)} \delta_{n0}. \tag{51}$$

Also, by multiplying Eq. 50 by ρ^2 and integrating over $[0, r]$ we obtain

$$\sum_{n=1}^{\infty} \left[\frac{\mathbb{A}_n^{(0)}}{q_n} w_n^{(0)} + \frac{\mathbb{A}_n^{(d)}}{q_n} w_n^{(d)} \right] \frac{J_2(q_n r)}{q_n r} = -\frac{rA_0}{8} + \frac{p^{(0)}r}{i\omega\rho_0 8}. \tag{52}$$

Finally, the substitution of Eq. 51 into Eq. 52 gives the expression

$$P_0 = B_S w^{(d)} + \pi R^2 p^{(0)}, \tag{53}$$

where we have denoted

$$B_S = i\omega\rho_0 \pi R^2 \left\{ d - \frac{16}{r^3} \sum_{n=1}^{\infty} \frac{\mathbb{A}_n^{(0)}}{q_n^3} \frac{J_1(q_n r) J_2(q_n r)}{J_0^2(q_n R)} \right\}. \tag{54}$$

The pressure $p^{(0)}$ is obtained by employing the Hagen-Poiseuille solution for fully developed flow in a circular pipe as

$$p^{(0)} = -8\mu h \frac{R^2}{r^4} w^{(d)}. \tag{55}$$

In the model developed here it is assumed that the backplate oscillates and the perforated plate is fixed. For the case when the perforated plate oscillates and the backplate is fixed to the substrate, the pressure $p^{(0)}$ resulting from the damping inside the holes also contains a term due to the oscillation of the air in hole. Homentcovschi and Miles (2005) determined that for this case the pressure becomes

$$p^{(0)} = -8\mu h \frac{R^2}{r^4} \left(1 - i\omega\rho_0 \frac{r^2}{4\mu} \right) w^{(d)}$$

which affects the added mass coefficient but not the damping force.

Therefore, the total damping coefficient of a cell is given by the real part of the formula

$$B_T \equiv \frac{P_0}{w^d} = B_S - 8\pi\mu h \frac{R^4}{r^4}. \tag{56}$$

P_0 being the total pressure on the diaphragm inside the cell and w^d the normal velocity of the plate. This formula provides the total damping coefficient predicted by the model based on the Stokes approximation of the viscous flow equations. The first term in formula (56) represents the squeezed-film component and the second term is the total (direct + indirect) contribution of the hole (Homentcovschi and Miles 2004, 2005).

3.5 The damping and added mass forces

The force of the fluid on the vibrating plate can be separated in two components. The component

$$B_R = \text{real}(B_T) = \text{real}\left(\frac{P_0}{w^d}\right),$$

in phase with the plate velocity, determined mainly by pressure, acts as a damping force. The remaining component

$$B_I = \text{imag}(B_T) = \text{imag}\left(\frac{P_0}{w^d}\right)$$

which is 90° out of phase with respect to velocity, appears as a mass added to that of the plate itself. Physically, the first force component is contributed by the fluid which pushes the plate, while the second arises from the fluid carried along with it. For the case when the length of the holes is small, the resistance of the holes is negligible compared with the squeezed-film damping. Therefore, the pressure p^0 in formula (53) is assumed to be zero. As a result, the fact that Stokes flow may not become fully developed in the small length holes is avoided.

4 Numerical simulations

Numerical solutions to the N–S equations provide a means to verify the analytical solution and to assess the effects of the inertia, compressibility and time-dependence. For the analytic solution the model assumed the Stokes approximation to the momentum equations (neglecting inertia) with harmonic time-dependence and incompressible fluid behavior. As stated earlier, numerical simulations were performed using two different sets of model equations. The numerical solutions were obtained using the FEM.

4.1 Steady-state solution

The analysis by Zuckerwar (1978) and Homencovschi and Miles (2008) shows that for the case of microphones in the audio frequency range viscous damping is practically independent of frequency. The squeezed flow is driven periodically in time and, based on the above comments, can be analyzed from the point of view of steady-state response. As described in Sect. 2, the flow field is characterized by the velocity field in the air \mathbf{V} and the pressure P . For the first set of numerical simulations, the steady-state form of the N–S equations for an incompressible, viscous fluid are solved (Eqs. 1 and 2 with the time derivative of velocity neglected).

The computational domain used here is the axisymmetrical region shown in Fig. 3b. The bottom boundary corresponds to the diaphragm where the inflow/outflow condition $\mathbf{u} = (0, 0, w_0)$ is specified. A constant pressure ($p = 0$) outflow condition is specified along the top surface corresponding to the hole aperture. The no-slip condition is applied on solid surfaces (i.e., the wall of the hole and the lower surface of the backplate). Slip symmetry $\mathbf{V} \cdot \mathbf{n} = 0$ is specified along the outside cylindrical surface corresponding to the cell gap boundary. Finally, axisymmetry is specified along the central axis of the unit cell.

Solutions to the governing equations for the given axisymmetrical domain and specified boundary conditions were obtained using the Fluid Mechanics Application Module of the Comsol Multiphysics (Comsol 2009) commercial software package. The software uses the FEM for the spatial discretization of the governing equations (here in cylindrical-polar coordinates). The domain is discretized using triangular elements. The Comsol software employs an iterative procedure to solve the resulting discrete, nonlinear algebraic system of equations that result from the finite element approximation of the N–S equations. A homogeneous, unstructured mesh was employed for most of the domain with areas of refinement in the gap region and around the reentrant corner of the azimuthal domain. While the full N–S equations were solved, for the conditions of the model here, the nonlinear terms are relatively

small and accurate solutions are readily obtained. Grid convergence studies were performed starting with approximately 1,000 elements and using up to as many as 20,000 elements for the most refined meshes.

4.2 Viscous acoustic equations

The numerical model based on the steady-state N–S equations outlined in the previous section includes the nonlinear convective acceleration terms. It is also of interest to investigate the effect of compressibility. The second numerical model is based on solving the linear viscous acoustic Eqs. 5 and 6. This complex form of the governing equations is not one of the standard sets of model equations built into the COMSOL software. However, the software package provides the capability of introducing the weak form of the complex viscous acoustic equations and using the software to obtain the finite element approximation of the equation system and the appropriate linear, algebraic system solver. Specifically, the finite element solution procedure for the linear, viscous acoustic equations was obtained by modifying the NonIsothermal Stokes Flow Application Mode contained in MEMS module of the COMSOL software package (COMSOL 2009). This model neglects inertia but includes compressibility.

The linearized, viscous acoustic equations require the same boundary conditions be applied on the flow field variables. Thus, the no-slip boundary condition was imposed on solid walls by zeroing the tangential velocity components. The no-penetration condition specifying zero normal velocity is again prescribed for symmetry boundaries in the model (slip/symmetry). The velocity of the vibrating plate is specified for the inflow boundary and, finally, the pressure is given on the outflow part of the boundary of the flow domain.

4.3 Model comparison results

Here, we present a set of representative results to compare the analytical solution and predictions from the two numerical models: steady-state N–S and the linear, viscous acoustic equations. Results were obtained for a unit cell with geometrical dimensions: $r = 3.39 \mu\text{m}$, $R = 5.64 \mu\text{m}$, $d = 1.6 \mu\text{m}$, $h = 15 \mu\text{m}$. These are the effective geometrical dimensions corresponding to the test structures *E* and *F* in Somà and De Pasquale (2007, 2008) and the test structures labeled topology 33 and 34 (for silicon samples) by De Pasquale et al. (2010). The perforated microstructure labeled *F* has 36×24 perforations and the value of the measured total damping coefficient is $C_F^M = 67.44 \times 10^{-6} \text{Ns/m}$. For the air in the unit cell, the following

property values are used: density $\rho_0 = 1.155 \text{ kg/m}^3$ and dynamic viscosity $\mu = 1.85 \times 10^{-5} \text{ Ns/m}^2$.

The axi-symmetrical form of the viscous acoustic equations were solved for a range of frequencies from 1 kHz to 1 MHz. The total force acting on the vibratory plate (having 846 holes) is composed of the viscous damping (the real part) and the added mass force (the imaginary part). The results given by the analytical formula (56) from the incompressible Stokes approximation for the viscous damping coefficient give the value $C_F^A = 69.33 \times 10^{-6} \text{ Ns/m}$ for the total damping coefficient (shown as \bullet - in Fig. 4) and the line shown as (\blacktriangle -) for the total added mass force coefficient.

The FEM solution of the viscous acoustic equations gives the total damping coefficient shown as the solid line (—) in Fig. 4 and the total added mass force coefficient drawn as the dashed line (---) in the same figure. Finally, the measured value of the total damping coefficient from Somà and De Pasquale (2007) and De Pasquale et al. (2010) is denoted by the dash-dot-dash (- · -) line parallel to the x-axis in Fig. 4.

From the results presented in Fig. 4, the following observations can be made: (i) The FEM (viscous acoustic equations) value for the total damping coefficient is reasonably well approximated by the constant value obtained from the analytical solution assuming incompressible Stokes flow over the whole range of frequencies considered (1 kHz to 1 MHz). (ii) For smaller frequencies $f < 0.5$ MHz, the same FEM value of the total damping force coefficient is very well approximated by the experimental measurement value. This demonstrates that compressibility effects are not significant for lower frequencies. (iii) The over prediction for values of the damping coefficient for frequencies higher than 0.5 MHz could be due to

completely neglecting rarefaction effects. (iv) Over the entire range of frequencies, the total added mass coefficient is much smaller than the corresponding total damping coefficient. For smaller frequencies, the predictions from the analytic solution and the FEM solution to the linear, viscous acoustic equations for the total added mass force are in reasonable agreement. However, the difference in the predictions from the two solution increases as the frequency increases indicating that compressibility is more important in determining the total added mass force. Over the entire frequency range, the analytical value overestimates the total added mass force.

The deviation between the analytical model and the numerical results for small frequencies is due to the simplified modeling of the pressure and velocity in the opening as uniform quantities. Better agreement may result by including in the analytical model more terms for approximating the velocity and the pressure in the opening.

5 Comparison to models using the Reynolds' equation

A set of numerical computations were performed to evaluate how well the analytic formula based on the Stokes equation model obtained in Sect. 3 compares to the FEM steady-state results. In each case, values for the damping coefficient obtained from Eq. 56 (solid line) are compared with the computed values obtained numerically (black circles) and with results obtained from a model using the Reynold's equation (dotted line) given by Homentcovschi and Miles (2007) (see also Homentcovschi and Miles 2004, 2005). The Reynold's approximation is based on computing the squeezed film damping using the lubrication approximation (Ševor's formula) and the direct and indirect resistances of the holes expressed in terms of the rim pressure, which is obtained via continuity arguments.

In Fig. 5 results for the damping coefficient $10^4 B$ are plotted versus the thickness of the backplate h for hole radius $r = 1 \mu\text{m}$, radius of the equivalent cylinder $R = 20 \mu\text{m}$ and two gap thicknesses $d = 1 \mu\text{m}$ and $d = 2 \mu\text{m}$. Results from the Reynold's equation are represented by the dotted lines, the solid lines correspond to the analytic Stokes equation model and the results from the steady N-S numerical model are shown as circles. The analytic solution, based on Eq. 56, is in excellent agreement with the FEM results. Also, for the parameter values of this case, the lubrication approximation results (i.e., the Reynold's equation) are in reasonable agreement with the present model predictions.

In Fig. 6, the damping coefficient B is plotted versus the equivalent cylinder radius R for gap thickness $d = 1 \mu\text{m}$ and thickness of the backplate $h = 8 \mu\text{m}$. Results are shown for three values of the hole radius: $r = 1 \mu\text{m}$,

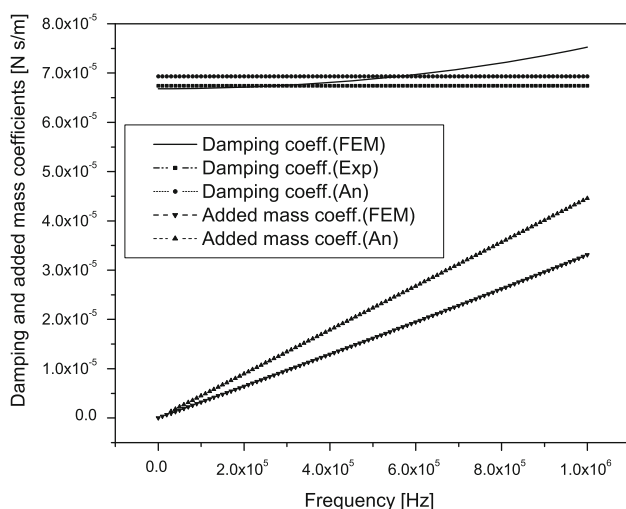


Fig. 4 Plots of the total damping and added mass coefficients versus frequency in the range 1 kHz–1 MHz

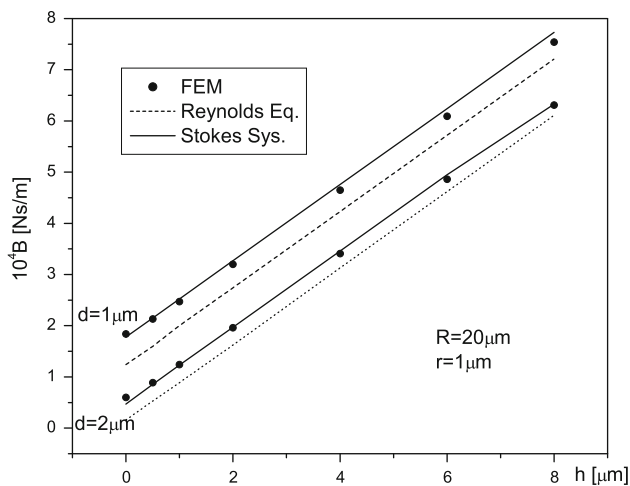


Fig. 5 The plot of the total damping coefficient versus backplate thickness h for $r = 1 \mu\text{m}$, $R = 20 \mu\text{m}$, and $d_0 = 1$ and $2 \mu\text{m}$

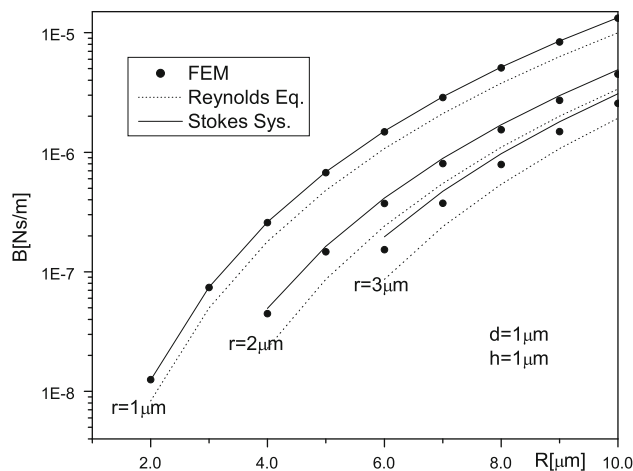


Fig. 7 The plot of the total damping coefficient B versus R for $r = 1, 2, 3 \mu\text{m}$, $d_0 = 1 \mu\text{m}$, and $h = 1 \mu\text{m}$

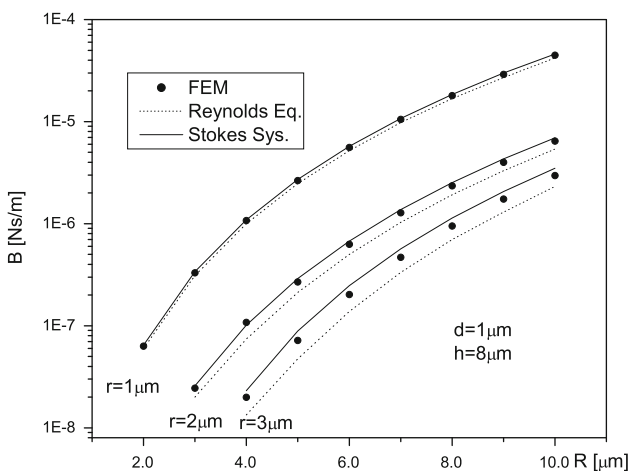


Fig. 6 The plot of the total damping coefficient B versus R for $r = 1, 2, 2.5 \mu\text{m}$, $d_0 = 1 \mu\text{m}$, and $h = 8 \mu\text{m}$

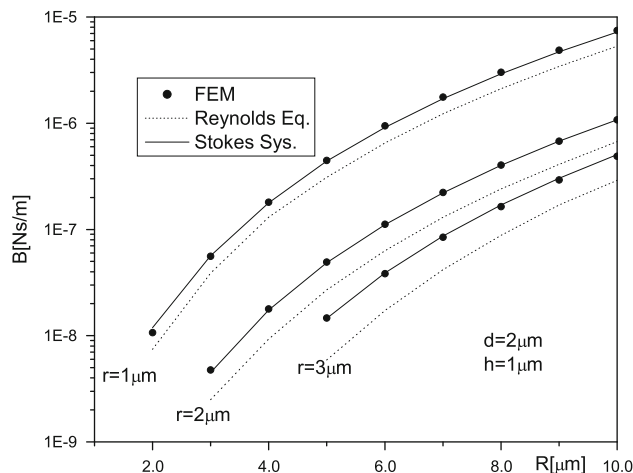


Fig. 8 The plot of the total damping coefficient B versus R for $r = 1, 2, 3 \mu\text{m}$, $d_0 = 2 \mu\text{m}$, and $h = 1 \mu\text{m}$

$r = 2 \mu\text{m}$, and $r = 3 \mu\text{m}$. For the smallest hole radius, all three solutions (FEM, analytic Stokes model, and the Reynolds' equation) are in excellent agreement. As the hole radius is increased, the predictions for the damping coefficient based on the lubrication approximation fall below those from the other two models, with the difference increasing with the hole radius r . In the last case ($r = 3 \mu\text{m}$), the analytic solution based on the Stokes approximation continues to agree well with the FEM simulation for $R > 6 \mu\text{m}$.

Figure 7 shows a plot of the damping coefficient versus radius of the equivalent cylinder R for the case where the backplate thickness equals the gap thickness, $h = d = 1 \mu\text{m}$, and values of the hole radius: $r = 1 \mu\text{m}$, $r = 2 \mu\text{m}$ and $r = 3 \mu\text{m}$. When the radius R of the equivalent cylinder is larger than about twice the diameter of the holes, the analytical solution given by formula (56) agrees well

with the damping coefficient obtained by the FEM solution. In all these cases, the Reynolds lubrication model predictions fall below the results from the other two models. Also, Figs. 6 and 7 suggest that the accuracy of the analytical approach as compared with that of the numerical method is independent of the backplate thickness h .

In the last case (Fig. 8), the gap thickness was increased to $d = 2 \mu\text{m}$, with all the other geometrical parameters the same as in Fig. 7. As seen from the figure, the same conclusions can be drawn as in the previous cases about the accuracy of the Reynolds' approach. On the other hand, the damping coefficients given by the analytical approach and the FEM solutions are in closer agreement than for the case where the gap equals $1 \mu\text{m}$ suggesting that the analytical method works better for gaps greater than $1 \mu\text{m}$.

We note that Fig. 5 uses a linear scale, while in Figs. 6, 7, and 8 a log scale is more appropriate for displaying the

damping coefficient. In all the cases considered, the results based on the Reynold's equation (including the direct and indirect resistances of the hole) underestimate the damping coefficient.

6 Comparison with measured damping coefficients for MEMS devices

Results for the damping coefficients from the analytical and numerical models developed here were compared to the published experimental data of De Pasquale et al. (2009, 2010). The experimental configuration consists of a central suspended plate covered with a pattern of square holes, connected to four lateral clamped supports of small cross-sectional area (refer to the references above for more details about the device configuration studied and the experimental setup and measurements). Both silicon and gold rectangular plates with different geometrical dimensions were fabricated. The geometrical dimensions of the test structures were obtained by profile measurements using an interferometric microscope. Six different rectangular configurations were studied for each plate material: four specimens with different hole cross-sectional area size and two with the same hole dimensions but different plate widths.

6.1 Results for gold samples

For rectangular gold plates, De Pasquale et al. (2009, 2010) present experimental results for six cases that they label as topology index 29–34. For the gold microstructures, the nominal plate thickness is $h = 6 \mu\text{m}$ and the air gap is $d = 3 \mu\text{m}$. Here, Table 1 gives the effective geometrical dimensions of the gold test structures. The second and the third columns contain the dimensions of the plate (the length L and the width W). As noted in the references, small differences between specimen nominal dimensions result from the fabrication process. Column four displays the number of holes ($M \times N$) in the rectangular plates in the length (M) and width (N) directions. The fifth column contains the measured damping coefficients C_M . In

columns six and seven of Table 1, we include the parameters b (the half-period of the structure) and $a = s_0/2$ (the half-length of a square hole side). Column eight contains the area ratio A (same as the perforation ratio q) of the structure and column nine contains the radius r of the circular cylinder which is equivalent to the square cross section of the square hole of the test specimen. Finally, the last column contains the radius R of the cylinder which represents the lower prism or gap region of the domain.

In De Pasquale et al. (2009, 2010) the quality factor is determined from the experimentally obtained curve of displacement versus frequency, and the damping coefficient is then calculated from the quality factor, frequency and the effective mass using the half-power bandwidth method. As mentioned above, the values of the measured damping coefficients, labeled as C_M are given in column 5 of Table 1. The experimental data for the six cases were given in Table V of De Pasquale et al. (2009), as well as in Table 2 of De Pasquale et al. (2010).

From the results for the unit cell geometry presented here, the damping coefficient of the whole structure is determined by multiplying the damping coefficient for a cell by the number of cells ($M \times N$) of the microstructure. Figure 9 is a plot of the relative error between predicted values of the damping coefficient and the measured values (listed in Table 1) for each of the experimental geometries denoted by the topology index. The relative error for three different models are shown in the figure. The results obtained from the analytical model developed in Sect. 3, C_{AN} , are plotted as open circles. The relative errors of the results given by the finite element solutions described in Sect. 4.1 (steady, incompressible N–S equations) are shown in Fig. 9 as full circles. Finally, the full squares correspond to the relative errors of the compact model presented by De Pasquale et al. (2009) with respect to the measured values. First, it is noted that the results given by the analytical formula and numerical approach track very well, with the absolute relative error between them being less than 7%. In addition, the results shown in the figure indicate that generally the relative error between the predictions from the compact model and the measured values is larger.

Table 1 The geometry of the measured and the calculated rectangular gold microstructure

Topolog index	L (μm)	W (μm)	$M \times N$	$C_M (10^{-6} \text{Ns/m})$	$b (\mu\text{m})$	$a (\mu\text{m})$	$A (\%)$	$r (\mu\text{m})$	$R (\mu\text{m})$
29	376.1	96.66	18×4	28.678	9.90	3.61	12.5	3.95	11.17
30	366.47	96.50	18×4	20.023	9.91	4.65	20.7	5.09	11.18
31	376.81	96.63	18×4	10.949	9.92	5.35	27.33	5.85	11.19
32	376.47	96.61	18×4	7.507	9.91	6.30	38.0	6.89	11.18
33	376.44	156.9	18×7	52.135	9.91	3.61	12.48	3.95	11.18
34	376.13	277.0	18×13	169.515	9.90	3.60	12.44	3.94	11.17

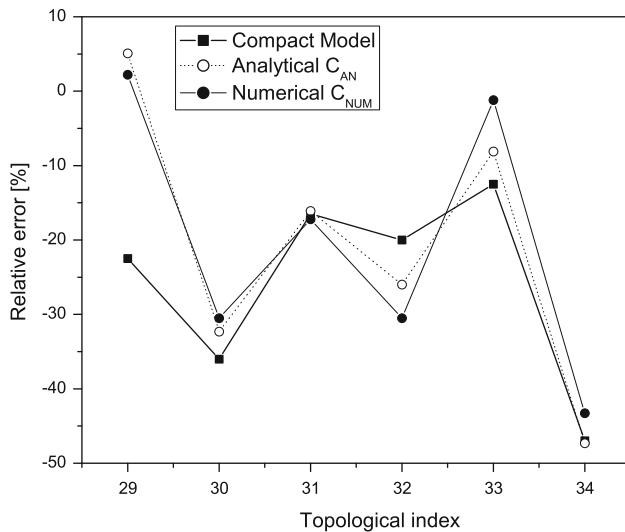


Fig. 9 The plot of the relative error with respect to the measured data (De Pasquale et al. 2009) of the damping coefficients for gold samples

The large relative errors of the all the models for some of the gold samples indicate that viscous damping significantly underestimates the measured damping coefficient, which in turn suggests that the observed damping of resonating gold structures may not be explained with a viscous damping model alone. Effects such as anchor losses, thermoelastic damping, structural dissipation (crystallographic defects), and bending of the relatively thin gold plates can contribute to the actual damping of the devices.

6.2 Comparison for silicon microstructures

The predictions for the damping coefficients from the analytical model and the steady-state FEM approach developed here were compared to the measurements for silicon microstructures reported by Somà and De Pasquale (2007), Veijola et al. (2008, 2009), and De Pasquale et al. (2010). (The measured results published by Somà and De Pasquale 2008 are slightly different but the main conclusion still holds).

The experimental set-up, the plate structure, and the analysis performed in these articles are essentially the same as those for the gold samples. For the experiments conducted with the silicon plates, the nominal thickness is $h = 15 \mu\text{m}$ and the air gap is $d = 1.6 \mu\text{m}$. In all but the most recent reference above, the data for six silicon samples are labeled using the letters A to F, which will be used here. However, in the recent article by De Pasquale et al. (2010), these six cases are designated by the topological index 29–34 similar to the gold samples discussed above.

Table 2 contains the geometrical parameters for the six experimental microstructures tested. In Table 3, the values

Table 2 The geometry of the measured and calculated silicon microstructures

Type	L (μm)	W (μm)	$M \times N$	$L:W$	b (μm)	a (μm)	A (%)	r (μm)	R (μm)
A	372.4	66.4	36×6	6:1	5.1	2.5	24	2.73	5.75
B	363.9	63.9	36×6	6:1	5.0	3.05	37	3.34	5.64
C	373.8	64.8	36×6	6:1	5.15	3.65	50	4	5.81
D	369.5	64.5	36×6	6:1	5.1	3.95	59	4.23	5.75
E	363.8	123.8	36×12	3:1	5.0	3.1	38	3.39	5.64
F	363.8	243.8	36×24	3:2	5.0	3.1	38	3.39	5.64

of the measured damping coefficients, labeled as C_M are given in column 2 for all six cases studied. Note that this column coincides with the second column in Table 2 of De Pasquale et al. (2010). Column three of Table 3 here contains the analytical damping coefficient of the whole structure C_{AN} , determined by multiplying the damping coefficient for the unit cell by the number of cells ($M \times N$) of the microstructure. The corresponding relative error compared with the measured values are given in parentheses. The last column contains the calculated damping coefficients C_{NUM} from the steady-state finite element model. Again, the damping coefficient of the whole structure is obtained by summing over the total number of cells. The relative error in the damping coefficient for the calculated values for the entire structure when compared to the measured values are given in parentheses. The results given by analytical approach and the steady, incompressible finite element model are in relatively close agreement with the measured values for all six microstructure samples. Also, the analytical and FEM predictions are closer to the measured values than those given by the compact models contained in the references listed above.

The results in Table 3 show that for the silicon microstructures, viscous damping models explain the measured quality factors for fabricated samples with sufficient accuracy, indicating that viscous damping is more important than anchor losses and surface bending effects in this case.

7 Conclusions

A model has been presented to describe the fluid flow in a unit cell of a periodic MEMS microstructure. In the model, the actual periodic unit cell structure of common devices (square or hexagonal prisms) is approximated by an equivalent axi-symmetrical cylindrical flow domain.

Analytical and numerical approaches for obtaining the viscous damping in a periodic unit cell flow domain have been developed. The analytical solution is based on the Stokes approximation of the N–S equations for viscous, incompressible flow (Sect. 3). A numerical treatment

Table 3 The measured (De Pasquale et al. 2010) analytical and numerical damping coefficients and the relative errors (in parentheses)

Type	C_M measured (10^{-6} Ns/m)	C_{AN} —rel. err. (10^{-6} Ns/m)	C_{NUM} —rel. err. (10^{-6} Ns/m)
A	47.38	40.81 (−13.87%)	40.71 (−14.08%)
B	19.46	18.30 (−5.96%)	17.86 (−8.22%)
C	9.863	10.76 (9.09%)	10.22 (3.62%)
D	7.609	8.095 (6.39%)	7.66 (0.67%)
E	38.22	34.67 (−9.30%)	33.77 (−11.6%)
F	67.44	69.33 (2.8%)	67.54 (0.15%)

employing the FEM was used to solve the steady-state N–S equations to verify the analytic solution and show that inertia terms in the N–S equations are not important. The FEM was also used to solve the linear, viscous acoustic equations to account for the influence of compressibility with the assumption of time harmonic behavior.

Values for the damping coefficients obtained from the analytical and numerical models developed here are found to compare well. Results for the total damping coefficient from the analytical model, which is based on incompressible fluid behavior, agree well with the linear, compressible viscous acoustic equation FEM results over a large range of frequencies (1 kHz to 1 MHz), indicating that an incompressible flow model is valid in this range of frequencies. The predicted values for the total added mass coefficient from the incompressible and compressible flow models differ as the frequency increases, with the compressible flow model yielding smaller values than the incompressible model.

The predictions for the damping coefficients for an air gap equal to 1 μm from the analytical and numerical incompressible models were compared and found to be in good agreement as long as the diameter of holes is smaller than the radius of the equivalent base cylinder, which is found to be the case when the area ratio, A , is less than approximately 0.25. The results from the analytical and numerical approaches developed here were also compared to a model based on the lubrication approximation (i.e., the Reynold’s equation). These results were found to agree with the present models only in the case where the radius of the equivalent cylinder is approximately 20 times larger than the radius of the hole when the thickness of the backplate less than 10 μm and in the case of small holes ($r = 1 \mu\text{m}$) and thick backplate ($h = 8 \mu\text{m}$). When these restrictions are not satisfied, the results from the Reynold’s equation fall below the values obtained from both the models developed in the present work.

The analytic formula obtained for the total damping coefficient provides a useful tool for use in the design of perforated microscale devices for certain applications. The analytical formulas obtained here for the damping and added mass coefficients have been validated by comparison to finite element solutions to the incompressible N–S equations for the unit cell model geometry. Despite its

simplicity, the analytical model yields damping coefficients in closer agreement with the measured values from available experimental data than predictions from compact models which require additional fitting parameters be prescribed. For larger air gaps (i.e., on the order of $d = 2 \mu\text{m}$) good agreement was obtained with the experimental data for hole diameters larger than the radius of the basic cell.

The main limitations of the given analytical formula are completely neglecting rarefaction effects and the hypothesis of uniform velocity and pressure in the opening. Also, due to the cylindrical approximation of the periodic cell the final formula works well only for small and medium values of area ratio. Finally, the formula for the damping coefficient of a cell has to be completed by a border effect calculation for cells which are at the sides of the MEMS microstructure.

Acknowledgments This work has been supported by the National Institute On Deafness And Other Communication Disorders grant R01DC005762-05 for a NIH Bioengineering Research Partnership and by Grant Number R01DC009429 to RN Miles (E-mail: miles@binghamton.edu). The content is solely the responsibility of the authors and does not necessarily represent the official views of the National Institute On Deafness And Other Communication Disorders or the National Institutes of Health.

Appendix: Bessel function relationships

In this appendix, we prove the relationships (64) and (67) which are used in Sect. 3. We begin with the Fourier-Bessel series associated with the function $f(\rho)$

$$f(\rho) = \frac{R^2 [J_0(q_m R)]^2}{2} \sum_{m=0}^{\infty} \tilde{f}_m J_1(q_m \rho) \tag{57}$$

where q_m is the m th root of the equation

$$J_1(q_m R) = 0. \tag{58}$$

The expansion coefficients are given by the expression

$$\tilde{f}_m = \int_0^R \rho f(\rho) J_1(q_m \rho) d\rho. \tag{59}$$

Also, for the Dini’s series of Bessel functions

$$h(\rho) = \frac{R^2 [J_0(q_m R)]^2}{2} \sum_{m=0}^{\infty} \hat{h}_m J_0(q_m \rho), \quad (60)$$

the expansion coefficients \hat{h}_m are determined by the formula

$$\hat{h}_m = \int_0^R \rho h(\rho) J_0(q_m \rho) d\rho. \quad (61)$$

The expressions (59) and (61) can be obtained using relationships given by Watson (1966, p. 580).

Coefficient calculation

First, in the case of the function

$$f(\rho, r) = \begin{cases} \rho, & 0 \leq \rho < r \\ 0, & r < \rho < R \end{cases} \quad (62)$$

the following integral expression is obtained

$$\tilde{f}(q_i, r) = \int_0^r \rho^2 J_1(q_i \rho) d\rho = r^3 \int_0^1 t^2 J_1(q_i r t) dt \quad (63)$$

The evaluation of the last integral is given by formula [6.567(1)] in Gradshteyn and Ryzhik (1994) which yields:

$$\tilde{f}(q_i, r) = r^3 \frac{J_2(q_i r)}{q_i r} \quad (64)$$

Second, in the case of the function

$$h(\rho, r) = \begin{cases} 1, & 0 \leq \rho < r \\ 0, & r < \rho < R \end{cases} \quad (65)$$

the following integral expression is obtained

$$\hat{h}(q_i, r) = \int_0^r \rho J_0(q_i \rho) d\rho = r^3 \int_0^1 t J_0(q_i r t) dt \quad (66)$$

In this case, the last integral is given by formula [6.567(9)] in Gradshteyn and Ryzhik (1994):

$$\hat{h}(q_i, r) = r^2 \frac{J_1(q_i r)}{q_i r} \quad (67)$$

References

- Bao MH (2000) Micro-mechanical transducers. Elsevier, Amsterdam
- Bao M, Yang H, Sun Y, French PJ (2003) Modified Reynold's equation and analytical analysis of squeeze-film air damping of perforated structures. *J Micromech Microeng* 13:795–800
- Bao M, Yang H (2007) Squeeze film air damping in MEMS. *Sens Actuators A* 136:3–27
- Bergquist J (1993) Finite-element modelling and characterization of a silicon condenser microphone with a highly perforated back-plate. *Sens Actuators A* 39:191–200

COMSOL Multiphysics User's Guide. Version 3.5, <http://www.comsol.com>

- De Pasquale G, Veijola T, Soma A (2009) Gas damping effect on thin vibrating gold plates: experiments and Modeling. In: *Proceedings of DTIP*, Rome, Italy
- De Pasquale G, Veijola T, Soma A (2010) Modelling and validation of air damping in perforated gold and silicon MEMS plates. *J Micromech Microeng* 20(015010):12
- Gerlach-Mayer UE (1991) Micromachined capacitive accelerometer. *Sens Actuators A* 25–27:555–558
- Gradshteyn IS, Ryzhik IM (1994) Table of integrals, series, and products. Academic Press, New York
- Homentcovschi D, Miles RN (2004) Modelling of viscous damping of perforated planar micromechanical structures. *Applications in acoustics. J Acoust Soc Am* 116:2939–2947
- Homentcovschi, Miles RN (2005) Viscous damping of perforated planar micromechanical structures. *Sens Actuators A* 119:544–552
- Homentcovschi D, Miles RN (2007) Viscous microstructural dampers with aligned holes: design procedure including the edge correction. *J Acoust Soc Am* 122:1556–1567
- Homentcovschi D, Miles RN (2008) Analytical model for viscous damping and the spring force for perforated planar microstructures acting at both audible and ultrasonic frequencies. *J Acoust Soc Am* 124:175–181
- Mattila T, Häkkinen P, Jaakola O, Kiihamäki J, Kyyrääinen J, Oja JA, Seppä H, Seppälä P, and T. Sillanpää (2000) Air damping in resonant micromechanical capacitive sensors. In: *14th European conference on solid-state transducers (EUROSENSORS XIV)*. Copenhagen, pp 221–224
- Mohite SS, Sonti VR, Pratap R (2008) A compact squeeze-film model including inertia, compressibility, and rarefaction effects for perforated 3-D MEMS Structures. *J Microelectromech Syst* 17:709–723
- Mohite SS, Kesari VH, Sonti R, Pratap R (2005) Analytical solutions for the stiffness and damping coefficients of squeeze films in MEMS devices having perforated back plates. *J Micromech Microeng* 15:2083–2092
- Pandey AK, Pratap R (2008) A comparative study of analytical squeeze film damping models in rigid rectangular perforated MEMS structures with experimental results. *Microfluid Nanofluid* 4:205–218
- Škvor Z (1967) On acoustical resistance due to viscous losses in the air gap of electrostatic transducers. *Acustica* 19:295–299
- Somà A, De Pasquale G (2007) Identification of test structures for reduced order modeling of the squeeze film damping in MEMS. In: *Proceedings of the DTIP symposium on design, test, integration and packaging of MEMS & MOEMS*
- Somà A, De Pasquale G (2008) Numerical and experimental comparison of MEMS suspended plates dynamic behaviour under squeeze film damping effect. *Analog Integr Circ Sig Process* 57:213–224
- Starr JB (1990) Squeeze-film damping in solid-state accelerometers. In: *Technical digest IEEE solid state sensor and actuator workshop*, Hilton Head Island, South Carolina
- Veijola T, Mattila T (2001) Compact squeezed-film damping model for perforated surface. In: *Proceedings of the transducers 2001*, München, Germany
- Veijola T (2006a) Analytic damping model for an MEM perforation cell. *Microfluid Nanofluid* 2:249–260
- Veijola T (2006b) Analytic damping model for a square perforation cell. In: *Proceedings of the 9th international conference on modeling and simulation of microsystems*, vol 3, pp 554–557
- Veijola T, Raback P (2007) Methods for solving gas damping problems in perforated microstructures using a 2D finite-element solver. *Sensors* 7:1069–1090

- Veijola T, De Pasquale G, Somà A (2008) Comparison between damping coefficients of measured perforated structures and compact models. In: Proceedings of DTIP, Nice
- Veijola T, De Pasquale G, Somà A (2009) Experimental validation of compact damping models of perforated MEMS devices. *Microsyst Technol* 15:1121–1128
- Watson GN (1966) *A treatise on the theory of Bessel functions*, 2nd ed. Cambridge University Press, London
- Wu MS, Vail EC, Li GS, Yuen W, Chang-Hasnain CJ (1996) Widely and continuously tunable micromachined resonant cavity detector with wavelength tracking. *IEEE Photon Technol Lett* 8:98–100
- Zuckerwar AJ (1978) Theoretical response of condenser microphones. *J Acoust Soc Am* 64:1278–1285